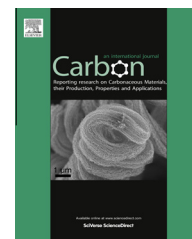


Available at www.sciencedirect.com

ScienceDirect

journal homepage: www.elsevier.com/locate/carbon

Electron-beam-induced direct etching of graphene

Cornelius Thiele^{a,b,*}, Alexandre Felten^{a,c}, Tim J. Echtermeyer^e, Andrea C. Ferrari^e,
Cinzia Casiraghi^{c,d}, Hilbert v. Löhneysen^{b,f,g}, Ralph Krupke^{a,b,h}

^a Institut für Nanotechnologie, Karlsruhe Institute of Technology, 76021 Karlsruhe, Germany

^b DFG Center for Functional Nanostructures (CFN), 76028 Karlsruhe, Germany

^c Physics Department, Free University Berlin, 14195 Berlin, Germany

^d School of Chemistry and Photon Science Institute, University of Manchester, Manchester M13 9PL, United Kingdom

^e Cambridge Graphene Centre, University of Cambridge, Cambridge CB3 0FA, United Kingdom

^f Physikalisches Institut, Karlsruhe Institute of Technology, 76128 Karlsruhe, Germany

^g Institut für Festkörperphysik, Karlsruhe Institute of Technology, 76021 Karlsruhe, Germany

^h Institut für Materialwissenschaft, Technische Universität Darmstadt, 64287 Darmstadt, Germany

ARTICLE INFO

Article history:

Received 21 March 2013

Accepted 12 July 2013

Available online 17 July 2013

ABSTRACT

We present electron-beam-induced oxidation of single- and bilayer graphene devices in a low-voltage scanning electron microscope. We show that the injection of oxygen leads to targeted etching at the focal point, enabling us to pattern graphene with a resolution of better than 20 nm. Voltage-contrast imaging, in conjunction with finite-element simulations, explain the secondary-electron intensities and correlate them to the etch profile.

© 2013 Elsevier Ltd. All rights reserved.

1. Introduction

Various chemical and physical approaches have been explored to pattern graphene [1–5]. The most common technique is oxidative plasma etching, usually performed while protecting part of the graphene sheet with a lithographic mask, reaching patterning precision in the nanometer range [5]. However, photomask residues often influence the resulting device characteristics, for example the doping level [6,7]. This problem can be avoided by using direct (maskless) lithography. This has been implemented using high-energy electrons from a transmission electron microscope (TEM) [8] or helium and neon ions from scanning ion beam microscopes [9,10]. These approaches allowed to reach a resolution of ~7 nm [10]. An alternative maskless approach relies on scanning-probe lithography methods [11,12]. This employs electrochemical etching in an ambient atmosphere and allows resolutions down to a few nanometers using an STM-based approach [12]. However, maskless lithography methods using a TEM or scanning helium/neon ion microscope suffer from

relatively high cost, and scanning probe methods usually are not well suited for upscaling.

Here we present an alternative approach using a scanning electron microscope (SEM) with a gas injection system. This exploits reactive species produced by the interaction of an injected gas with the electron beam. The resolution is limited by the radius of the primary electron beam, which can be tuned down to the nanometer range for a typical SEM. The applicability of this technique was previously demonstrated for other materials, such as silicon oxide, silicon nitride, carbon nanotubes (CNTs) and sputtered carbon thin films [13–18], and has been named electron-beam-induced etching/oxidation (EBIE/EBIO). In each case a different gas was used, e.g., xenon difluoride for silicon oxide [13], water vapor for silicon nitride [14], and both water vapor [15,16] and oxygen [16–18] for single- and multi-walled CNTs and sputtered carbon thin films.

Nitrogen was used to etch nanopores into few-layer-graphene (FLG) in Ref. [19], however, the fabrication of extended structures was not studied. Here we implement EBIO

* Corresponding author.

E-mail address: Cornelius.Thiele@kit.edu (C. Thiele).

0008-6223/\$ - see front matter © 2013 Elsevier Ltd. All rights reserved.

<http://dx.doi.org/10.1016/j.carbon.2013.07.038>

for single-layer (SLG) and bilayer (BLG) graphene. We demonstrate targeted etching at the focal point and direct patterning of arbitrary designs with a resolution of ~ 20 nm. Voltage-contrast imaging combined with finite-element simulations allow us to explain the observed secondary-electron intensities and correlate them to the etch profile.

2. Experimental

Graphene samples are prepared by micromechanical cleavage of graphite onto doped Si substrates with 300 nm thermal oxide and pre-patterned gold markers [20]. SLG and BLG are identified by a combination of optical microscopy [21] and Raman spectroscopy [22]. Fig. 1 shows the typical Raman spectra of the flakes. The observed G peak position of 1586 cm^{-1} and full-width-at-half-maximum (FWHM) of 21 cm^{-1} indicate a doping level of less than $5 \times 10^{12}/\text{cm}^2$ of our as-prepared SLG [23]. The 2D peak for SLG samples is of Lorentzian shape and there is no discernible D peak. BLG can be identified by its characteristic 2D peak, which can be decomposed into four Lorentzians [22]. We then define electrical contacts with a pitch of 500 nm using standard electron-beam lithography with a PMMA mask, and metallization of Ti/Pd contacts. The doped Si substrate acts as backgate.

A Zeiss Ultra Plus SEM is used both for imaging and lithography. We use a voltage-contrast SEM technique [24] to acquire images. This technique consists in applying a positive voltage V_{gate} to the Si, while the metal contacts are grounded. This greatly improves the contrast between substrate and graphene, as it decreases the number of secondary electrons reaching the detector. The built-in charge-compensation needle is used to inject oxygen (purity 99.998%), less than $50\text{ }\mu\text{m}$ above the sample surface, $\sim 200\text{ }\mu\text{m}$ from the SEM focal point, as shown in the scheme in Fig. 2. The oxygen flow is dosed by a mass-flow controller and set to $\sim 22\text{ sccm}/\text{min}$. The overall system pressure is kept constant at $\sim 2.5 \times 10^{-3}\text{ mbar}$. These values represent a compromise between an acceptable etching speed and loss of resolution due to scattering of the primary electron beam by the gas molecules. For dose tests and pattern writing, a Raith Elphy lithography system is connected to the SEM. The acceleration voltage of primary-beam electrons is set to 3 kV, which ensures a large contrast between graphene and substrate even without voltage contrast.

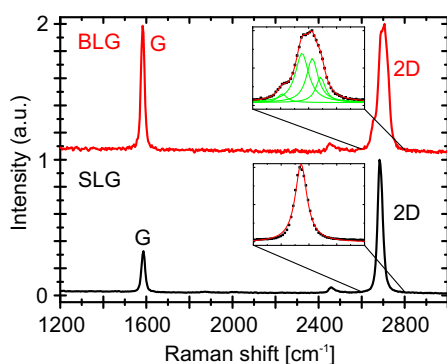


Fig. 1 – Raman spectra of our SLG and BLG flakes, measured at 514.5 nm excitation.

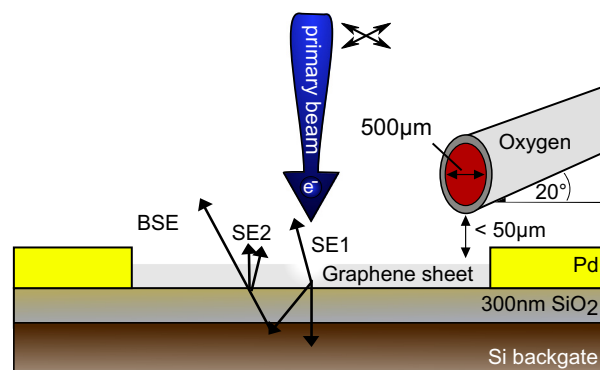


Fig. 2 – Schematic of the EBIO setup: primary-beam electrons are scanned across a graphene sheet on a SiO_x/Si substrate, leading to secondary-electron emission (SE1, SE2), and backscattered electrons (BSE). The graphene sheet, which is contacted by Pd electrodes, is etched by radicals derived from injected oxygen.

This also avoids buildup of surface potential due to charging [25].

We select the slowest possible line scan speed (1.7 s/line scan, limited by the control software) to avoid overexposure of the initial leftmost spot of the desired line. This is necessary because of the synchronization between the scan generator and the beam blaster specific to the Zeiss SEM. The line scan is repeated in the same direction each time by blanking the beam after each line scan and resetting it to its starting position. When repeating the scan, a delay between the start of the scan and the release of the beam causes an overexposure of the starting spot. The accumulated deposited dose becomes significant relative to the line dose when the scan speed is set to a high value and the beam is reset many times per second.

3. Results

Repeated line scans under oxygen flow produce cuts across SLG and BLG, as shown in Fig. 3. The cut in the SLG is typically ~ 30 nm wide, as shown in Fig. 3a. The magnification is chosen such that the line scan covers the sample's full width and extends beyond by at least ~ 200 nm, so to exclude any residual effect due to the delay of the scan generator, as discussed in Section 2.

In order to monitor the progress of cutting, the low-bias conductance of a SLG/BLG segment is continuously monitored during line scans. The line scans are stopped when the conductance falls below our measurement limit ($\sim 10^{-9}\text{ }\Omega^{-1}$). The currents through SLG and BLG during cutting are shown in Fig. 4. In the SLG sample the conductance initially increases up to an exposure dose of $\sim 4\text{ mC}/\text{m}$, then starts to drop. Line scans are stopped at $\sim 8\text{ mC}/\text{m}$, when the conductance reaches the noise level of our measurement setup. We take this as the indication that the initial sample has separated into two segments. This is confirmed by direct SEM imaging, which shows a gap of ~ 30 nm, Fig. 3a.

The identical process is used on BLG, Fig. 3b. In this case, a widening of the cut from the BLG center towards the edge is

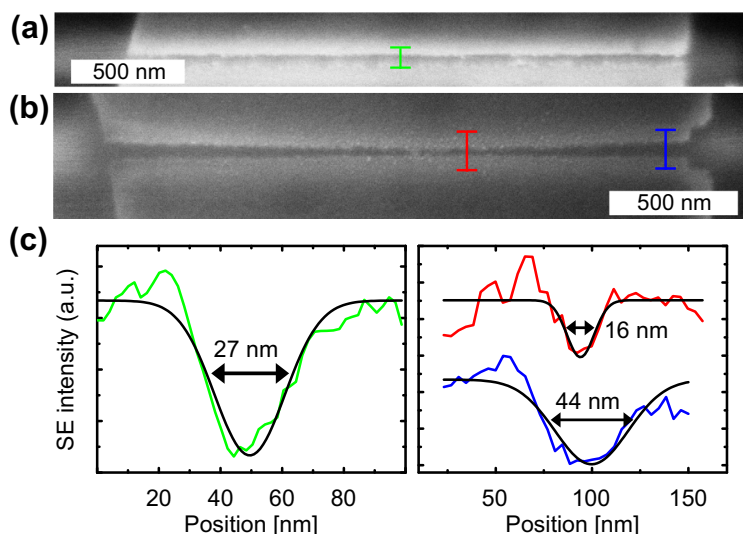


Fig. 3 – (a,b) SEM images of cuts in (a) SLG and (b) BLG. (a) acquired at $V_{\text{gate}} = 20$ V (b) acquired at $V_{\text{gate}} = 10$ V. (c) SE intensity profiles perpendicular to the trenches at marked positions, fitted by inverse Gaussian curves. Corresponding FWHMs are given.

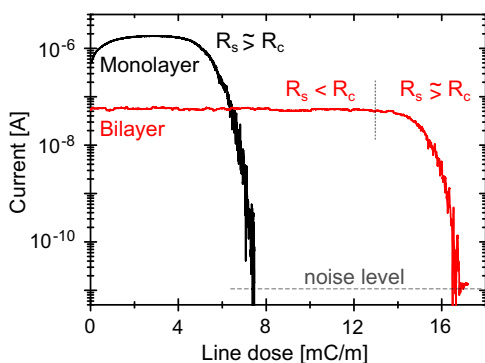


Fig. 4 – Current through SLG/BLG segment at 5 mV bias and $V_{\text{gate}} = 0$ vs. line dose for the cutting processes in Fig. 3a and b. Regions of different ratios of sheet and contact resistances R_s and R_c are indicated.

observed. The cut width approximately doubles going from the center towards the edges. At the center, the width is ~ 20 nm, comparable to that observed in the SLG case. The electrical data in Fig. 4 show that, unlike the case of SLG, there is no initial increase in the conductance, but the conductance stays constant up to a dose of ~ 14 mC/m, then rapidly drops to the noise level. We ascribe this to different initial doping levels of the SLG and BLG devices, with the Dirac point shifting more for the SLG device at the start of etching.

To study the intermediate state of a BLG cut, the process is interrupted before the onset of a conductance decrease. This experiment is performed for the device in Fig. 5. This picture, taken after 5 min, shows that etching already started at the BLG edges and progresses inwards. However, isolated defects at the BLG center can be seen as well. Fig. 6 plots secondary-electron intensity line-scan profiles recorded during another BLG cutting at different times. Three distinct levels can be seen for intermediate cutting times. The observation of steps



Fig. 5 – SEM image of a BLG segment after 5 min of cutting, acquired at $V_{\text{gate}} = 10$ V.

in the intensity, advancing towards the BLG center during the cutting process, allows us to identify the three levels with the signal of an intact BLG, of a BLG with the top layer already etched, and the substrate. After 8 min, only a small section of the top layer along the line scan remains, whereas the bottom layer appears to be almost completely intact. The top and bottom layers have hence been cut in sequence, similar to what was previously observed for oxygen plasma etching of BLG and FLG samples [26–28]. In this experiment, the total cutting process took 13.5 min.

Since our SLG and BLG segments have similar widths of $1.9 \mu\text{m}$ and $2.1 \mu\text{m}$, the total dose needed to cut them scales with the number of layers. To compare the etching speed, the different widths and the number of carbon layers need to be taken into account. The etching speed is the segment width divided by the cutting duration, times the number of layers. Using this, we calculate an etch speed of 2.5 nm/s from each edge towards the center for both devices, normalized to a line dose of $25 \mu\text{C}/\text{m}$ per second (100 pA beam current, $4 \mu\text{m}$ line scan width).

An SEM image of a dose test and of an arbitrary pattern on SLG is shown in Fig. 7a. Rectangular boxes with a 5 nm width and 600 nm height are used. Lower and upper dose test boxes are written with doses from 1.5 to $22.5 \text{ C}/\text{cm}^2$ increasing in steps of $1.5 \text{ C}/\text{cm}^2$ and 23–29 C/cm^2 with steps of $1 \text{ C}/\text{cm}^2$, respectively.

Up to $4.5 \text{ C}/\text{cm}^2$, a dark line is observed in the secondary electron image. This indicates hydrocarbon deposition, which

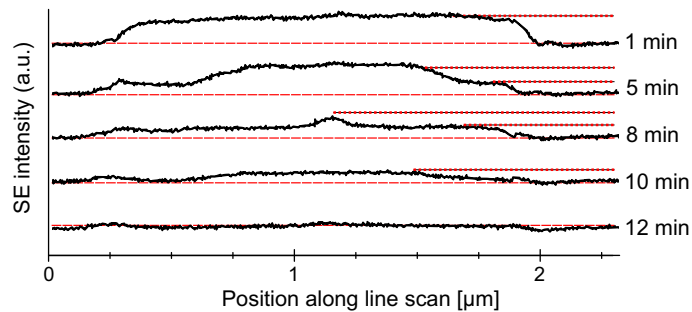


Fig. 6 – Sequential line scan profiles during the BLG cutting process shown in Fig. 3b, recorded at different times.

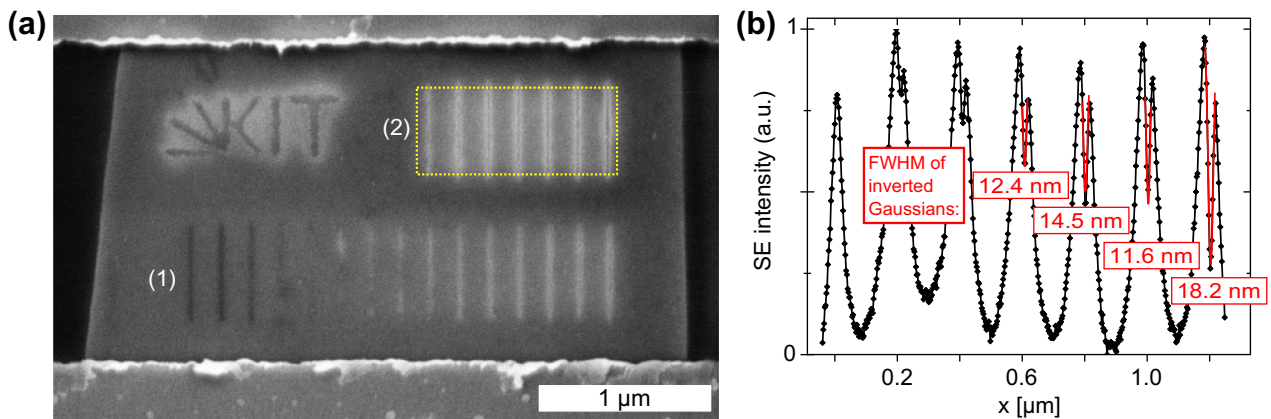


Fig. 7 – (a) SEM image of a dose test on SLG, comprising 5 nm wide boxes with a 200 nm pitch written with doses from (1) 1.5 to 22.5 C/cm² (1.5 C/cm² step) increasing from left to right, and (2) 23–29 C/cm² (1 C/cm² step). (b) Corresponding line profile of the secondary-electron intensity of dose test lines (2). The pixel values of the marked area of the SEM image are vertically binned. Peaks are fitted by a sum of two Gaussians: one to describe defect-induced SE emission enhancement caused by diffusing radicals with a FWHM of ~60 nm, and an inverted Gaussian with FWHM from 11.6 to 18.2 nm which describes the reduced SE emission of a narrow trench in the graphene sheet.

is likely even in presence of oxygen when the initial local concentration of hydrocarbons on the sample surface is high. Higher doses first lead to a brightening of the exposed area, indicating an increase in secondary electron emission. Then, above 23 C/cm², a dark feature appears in the line center, which we identify as reduced secondary-electron emission from a cut in the SLG.

4. Discussion

Electron-beam-induced oxidation is driven by the creation of reactive species in the injected gas or by oxygen gas adsorbed onto the surface. Reactive species include oxygen molecules in an excited state, ionized oxygen atoms or ozone. The cross-sections for electron collisions with oxygen molecules are in the range of 0.01 (dissociation) to 1 Å² (ionization) for electrons with kinetic energies of ~5 eV to several keV [29–31]. Given that our SEM operates at 3 kV we conclude that primary, secondary, and backscattered electrons have enough energy to produce many reactive species derived from oxygen.

While most of those electrons are created at the focal point of the primary beam, the radial distribution of escaping backscattered electrons from Si with 300 nm oxide using a 3 kV primary beam extends into the micrometer range. The

secondary electrons created by the primary-beam escape from a region around the focal point with a radius comparable to the mean secondary-electron escape depth, which is ~8 nm for SiO₂ [32].

The interaction of secondary electrons with the injected gas is a resolution-limiting factor for e-beam-induced deposition [33]. Surface and gas-phase diffusion also limit the resolution of gas-assisted processes inside the SEM. Reactive species can diffuse while they are physisorbed at the sample surface, and might not react with a carbon atom close to the focal point. The effect of this diffusion becomes important when the process is no longer limited by the generation of radicals under the beam (electron-flux limited), but rather by the supply of etchant (mass-transport limited) [13]. In this regime the etch profile would have the shape of a ring, with a low etch rate at the center and a higher one in the surrounding area [13], because of the concentric surface diffusion of adsorbed gas molecules. Since we do not see such a profile in Fig. 7, we assume that our parameters lie within the electron-flux-limited regime.

In the SLG current traces, an initial increase can be observed. This might be due to the charge-neutrality point moving away from zero. Electrostatic gating due to trapped charges as well as interfacial effects between substrate and

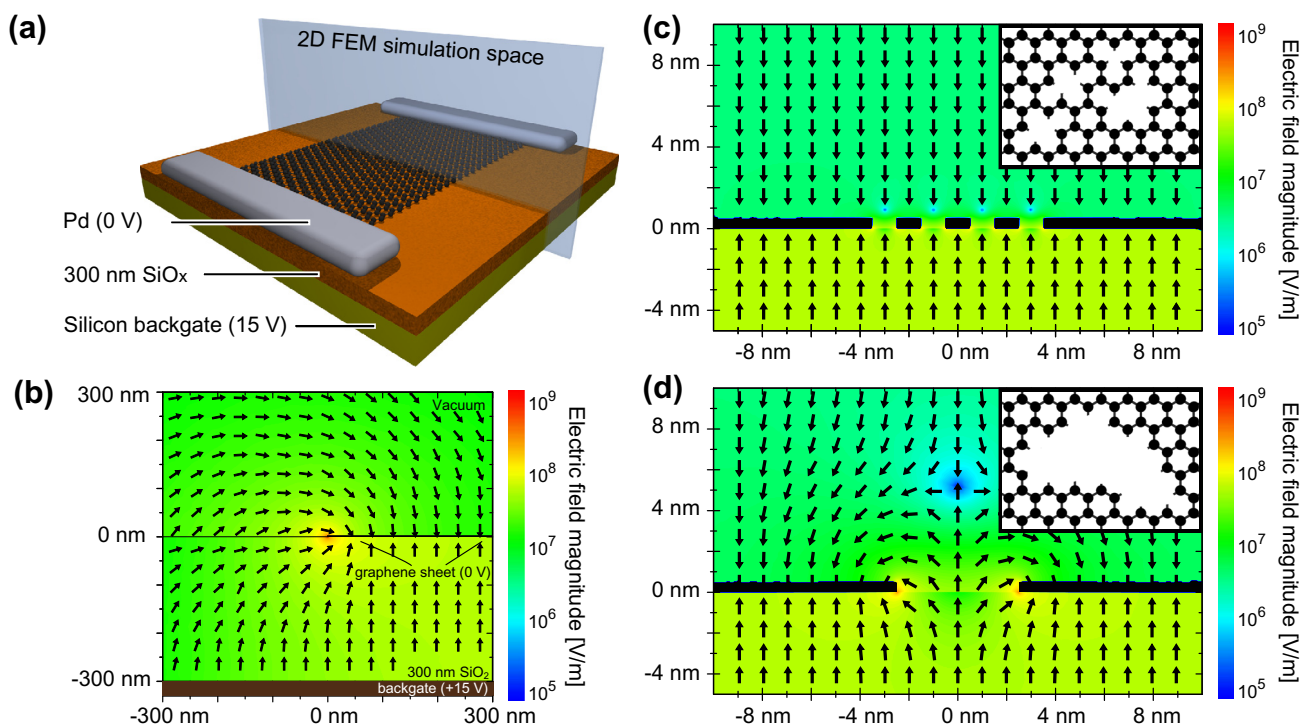


Fig. 8 – (a) Scheme of the two dimensional FEM simulation (not to scale). The simulation depicts a cross-section through a graphene device. The simulation extends well beyond the dimensions of the graphene sheet, with a width of $100\ \mu\text{m}$ and a height of $100\ \mu\text{m}$ (compared to the $5\ \mu\text{m}$ wide graphene sheet in our experiments), to exclude any boundary effects. The graphene sheet is lying on top of $300\ \text{nm}$ of silicon oxide on a silicon backgate, which is held at a potential of $+15\ \text{V}$. The graphene sheet is grounded ($V = 0$). (b) Electric field around the edge of the grounded graphene sheet. The field strength is highest at the edge. (c, d) Electric field near multiple 1-nm -sized holes (c) and a single 5-nm -sized hole (d). Note the different scale compared to (b). Except for the differences in the center of the sheet, all simulations are identical. Insets illustrate corresponding top-down views onto defective graphene sheets (not to scale).

SLG might also play a role. Eventually the current decreases down to the noise level. Except for the initial increase, the same trace is observed for BLG, consistent with the assumption of the sheets being etched from the edges towards the center, with the width of the central part of the sheet limiting the overall conductance. Line scans on SLG and BLG flakes show that their edges are more susceptible to electron-beam-induced etching than the sheet itself, as shown in Fig. 3. This is likely due to the presence of dangling bonds and an overall more chemically reactive nature of the graphene edges [34–36]. The enhanced electric field at SLG or BLG edges, which leads to enhanced secondary-electron emission, might also enhance the etch rate at the edges. Once the etching has started at the edges, it continues towards the center from both sides at the same etch speed, roughly $2.5\ \text{nm/s}$.

From the secondary-electron-intensity profiles in Fig. 6 we infer that, for a BLG, the top layer is almost completely etched before the bottom layer is attacked by the reactive species. This was observed before in plasma-based etching of multi-layer graphene [26–28]. Also, a widening of the cut at the edges is observed, due to secondary-electron emission from the surface and/or surface diffusion of reactive species. Once

a trench has formed in the sheet, material is also etched perpendicularly to the electron line scan, albeit at a reduced rate. Note that the symmetric BLG etch profile excludes drift as resolution-limiting factor in our setup.

To further analyze the SLG cuts and understand the corresponding secondary-electron images, a secondary-electron intensity profile (Fig. 7b) is extracted by vertically binning the pixel values of the dose test area marked in Fig. 7a. The enhanced secondary-electron emission around exposed sites can be fitted with a Gaussian curve with a full-width-half-maximum (FWHM) between $61.9\ \text{nm}$ and $67.9\ \text{nm}$ for the peaks shown. For doses higher than $23\ \text{C/cm}^2$, a dip within the intensity is seen, more pronounced at higher doses. These dips can be fitted by inverted Gaussians with a FWHM from 11.6 to $18.2\ \text{nm}$ for the data in Fig. 7b.

For the interpretation of SE images it is important to consider how local electric fields affect SE emission. Therefore we calculate the electric field of a SLG on Si/SiO_x with a positive voltage applied to the backgate, using the finite element (FE) simulation software FlexPDE v6¹. The two-dimensional simulation space consists of a $5\ \mu\text{m}$ wide and $3.5\ \text{\AA}$ high conducting layer, representative of a SLG sheet, on $300\ \text{nm}\ \text{SiO}_2$

¹ <http://www.pdesolutions.com>.

($\epsilon_r = 3.9$) with a width of 100 μm , both terminated by vacuum ($\epsilon_r = 1$). A backgate is placed beneath the oxide. The program gives the electric potential Φ in the electrostatic limit $\nabla(\epsilon\nabla\Phi) = 0$, where $\epsilon = \epsilon_0\epsilon_r$. In all simulations, the SLG potential and the backgate are set to zero and 15 V, respectively, because these values are our imaging conditions. To avoid an unnecessarily detailed computational grid over the whole simulation space, the adaptive mesh generator of the program was instructed to refine the mesh in each iteration only in the vicinity of the graphene sheet. This kept the number of computational cells manageable, i.e., below one million. Fig. 8a shows a three dimensional sketch of SLG on a substrate with metal contacts, with the two dimensional FEM simulation space indicated as a plane perpendicular to the substrate, intersecting the SLG sheet.

Fig. 8b plots the simulated electric-field magnitude $|E|$ around the SLG edge, with the direction of the electric field indicated by arrows. A large field enhancement is observed around the edge as the field lines curve around it. This leads to an increased secondary-electron emission, consistent with Fig. 3a. Topography alone cannot explain the large edge enhancement of secondary-electron emission, since the magnitude of topographic enhancement depends on the ratio of step height to the typical secondary-electron escape depth [37]. For silicon oxide, this escape depth is ~ 8 nm [32], therefore much larger than the step height of SLG. To further correlate the SE intensity distribution in Fig. 7b to features in the SLG topography, FE simulations are repeated, but with 1-nm (Fig. 8c) and 5-nm (Fig. 8d) holes in the SLG. Both Figs. 8c and d show the magnitude of the electric field (color scale) as well as its direction (arrows). Fig. 8c plots a simulation where, viewed from the top, several isolated holes are introduced in SLG in close proximity to each other. Fig. 8d represents a single larger hole.

The variation in electric-field distribution between Figs. 8c and d is significant. Multiple small holes modify the electric field close to the surface and in direct vicinity of the holes only. By comparing Fig. 8c with 7a, we identify this situation with an exposure dose of 23 C/cm² or less. Given a resolution of ~ 1.6 nm at 3 kV acceleration voltage of our SEM, this would be detectable only as a slight SE intensity enhancement due to the field effect at the SLG edges. Once the width of a cut is above a certain threshold, the electric field within the hole reverses (as seen by comparing Fig. 8d with 8c), because of the positively biased backgate. As the hole becomes larger, the neutral point in the electric field moves further away from the SLG. Secondary electrons are held back by this field and eventually a dip in intensity is observed in the electron microscope. This is precisely what was seen in the SEM images in Fig. 7a for doses higher than 23 C/cm². The average FWHM of the observed dips in intensity is 14.2 ± 3.0 nm, which we identify as our EBIO patterning resolution. This again correlates well with the escape radius of secondary electrons of type 1 (SE1) of silicon oxide.

Diffusion of radicals and secondary/backscattered electron effects are likely to cause the observed widening of the secondary-electron intensity profile around patterns and dose test rectangles. Diffusing radicals, as well as radicals created further away from the exposed site, might lead to an extended network of small defects in the SLG, which would then cause an increase in SE intensity around exposed sites.

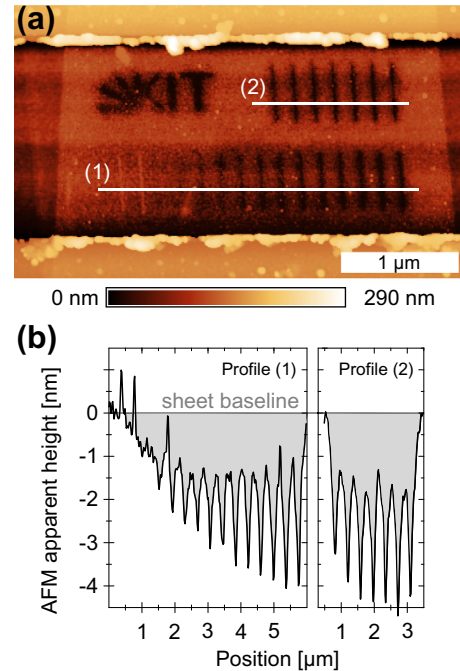


Fig. 9 – (a) AFM topography image of the dose test from Fig. 7a. (b) Corresponding line profiles. Low doses lead to hydrocarbon deposition, whereas higher doses create a cut in the graphene sheet. Removal of hydrocarbons as well as etching of the substrate lead to a trench depth of up to 4 nm.

To further support the analysis of the SE images, atomic force microscope (AFM) measurements are performed, Fig. 9. The two lines with doses ≤ 3 C/cm² show a slight protrusion, whereas for higher doses indentations are observed. The latter become deeper with increasing dose. The protrusions for low exposure doses confirm that e-beam irradiation initially leads to a deposition of hydrocarbons [38]. One would however not expect hydrocarbon deposition to occur at the focal point of electron-beam-induced oxidation, as there should be reactive species to counteract it. However, deposition and oxidation are competing processes. At the beginning of an etch process, the surface coverage with hydrocarbon residues is so high that cracking of hydrocarbons is more significant than generation of reactive oxygen species. This is supported by the sample topography in Fig. 9. We also note that the samples were handled in air and no special care was taken to clean the substrates from lithography residues.

The indentations for higher exposure are significantly deeper than expected for an SLG layer, which has a height of 0.35 nm. Typical height observations relative to an oxide surface are of the order of 1 nm [39]. To discriminate etching of graphene from etching into the substrate, an identical EBIO process is run on a substrate, see Fig. 10. This shows two effects: (1) formation of 1 nm deep trenches by etching of SiO₂ or oxygen removal from it, consistent with Ref. [40], (2) reduction of surface roughness near the exposed area due to removal of hydrocarbons. Repeating the process without oxygen injection, which simulates the imaging conditions, we observe large buildups of hydrocarbons on the surface, up to 2 nm in height. A combination of hydrocarbon buildup

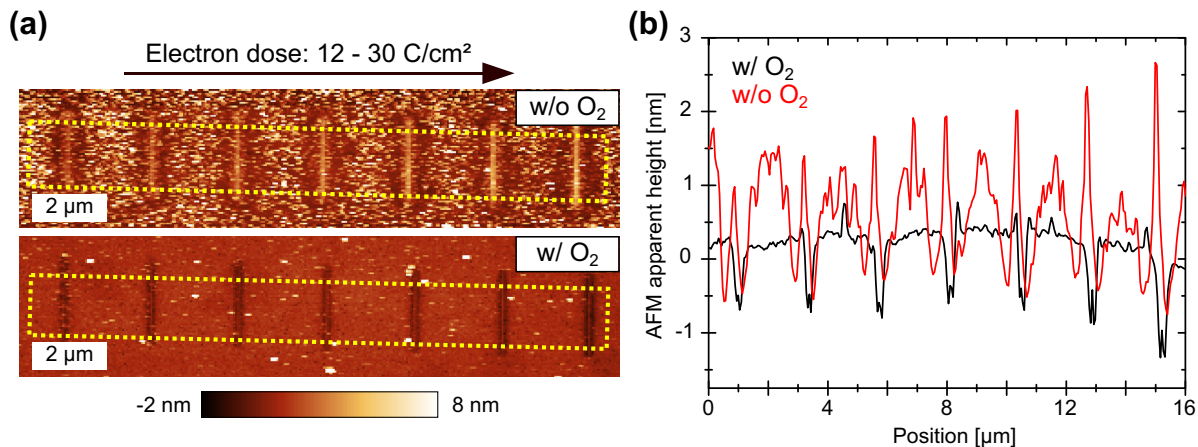


Fig. 10 – (a) AFM topography of electron-beam line scans with (bottom) and without (top) oxygen flow on 300 nm SiO_x on Si substrates. The electron dose increases from left to right from 12 to 30 C/cm², comparable to the doses used for cutting SLG. (b) Extracted line scan profiles from (a). Without oxygen injection, an increasingly higher protrusion is observed at the position of the line scan, with a height of up to 2.5 nm. In the presence of oxygen, diffusing radicals clean the surrounding area of the line scan from lithography residues and the substrate roughness decreases. Also, a clear depression is observed at the exposed area, up to 1 nm deep.

on top of or underneath the graphene (with both hydrocarbons and graphene being cut together) and the presence of a trench in the oxide explain the observed apparent graphene height of ~4 nm in the AFM topography.

5. Conclusions

We introduced electrically insulating cuts in mono- and bilayer graphene in a scanning electron microscope using electron-beam-induced oxidation. Arbitrary patterns can be written with a resolution better than 20 nm. Atomic force micrographs as well as detailed studies of the secondary-electron intensities over the exposed areas confirm the presence of cuts. This shows that electron-beam-induced oxidation can be used for rapid prototyping of graphene devices, e.g., ribbons, lattices, as well as for engineering graphene devices exhibiting steps such as mono-bilayer interfaces.

Acknowledgements

We acknowledge funding from the Karlsruhe Nano Micro Facility (KNMF), a Helmholtz Research Infrastructure at Karlsruhe Institute of Technology, the Alexander von Humboldt Foundation, ERC grant NANOPOTS, EPSRC grants EP/K01711X/1, EP/K017144/1, EU Grants RODIN and GENIUS, CareRAMM, a Royal Society Wolfson Research Merit Award and the Cambridge Nokia Research Centre.

Appendix A. Supplementary data

Supplementary data associated with this article can be found, in the online version, at <http://dx.doi.org/10.1016/j.carbon.2013.07.038>.

REFERENCES

- [1] Datta SS, Strachan DR, Khamis SM, Johnson ATC. Crystallographic etching of few-layer graphene. *Nano Lett* 2008;8:1912–5.
- [2] Han MY, Özyilmaz B, Zhang Y, Kim P. Energy band-gap engineering of graphene nanoribbons. *Phys Rev Lett* 2007;98:206805.
- [3] Schedin F, Geim AK, Morozov SV, Hill EW, Blake P, Katsnelson MI, et al. Detection of individual gas molecules adsorbed on graphene. *Nat Mater* 2007;6:652–5.
- [4] Ponomarenko LA, Schedin F, Katsnelson MI, Yang R, Hill EW, Novoselov KS, et al. Chaotic dirac billiard in graphene quantum dots. *Science* 2008;320:356–8.
- [5] Stampfer C, Güttinger J, Molitor F, Graf D, Ihn T, Ensslin K. Tunable Coulomb blockade in nanostructured graphene. *Appl Phys Lett* 2008;92:012102.
- [6] Dan Y, Lu Y, Kybert NJ, Luo Z, Johnson ATC. Intrinsic response of graphene vapor sensors. *Nano Lett* 2009;9:1472–5.
- [7] Cheng Z, Zhou Q, Wang C, Li Q, Wang C, Fang Y. Toward intrinsic graphene surfaces: a systematic study on thermal annealing and wet-chemical treatment of SiO₂-supported graphene devices. *Nano Lett* 2011;11(2):767–71.
- [8] Fischbein MD, Drndic M. Electron beam nanosculpting of suspended graphene sheets. *Appl Phys Lett* 2008;93:113107.
- [9] Bell D, Lemme M, Stern L, Williams J, Marcus C. Precision cutting and patterning of graphene with helium ions. *Nanotechnology* 2009;20:455301.
- [10] Winston D, Manfrinato VR, Nicaise SM, Cheong LL, Duan H, Ferranti D, et al. Neon ion beam lithography (NIBL). *Nano Lett* 2011;11:4343–7.
- [11] Tapasztó L, Dobrik G, Lambin P, Biro LP. Tailoring the atomic structure of graphene nanoribbons by scanning tunnelling microscope lithography. *Nat Nanotechnol* 2008;3:397–401.
- [12] Giesbers A, Zeitler U, Neubeck S, Freitag F, Novoselov K, Maan J. Nanolithography and manipulation of graphene using an atomic force microscope. *Solid State Commun* 2008;147:366–9.

- [13] Lassiter MG, Rack PD. Nanoscale electron beam induced etching: a continuum model that correlates the etch profile to the experimental parameters. *Nanotechnology* 2008;19:455306.
- [14] Spinney P, Howitt D, Smith R, Collins S. Nanopore formation by low-energy focused electron beam machining. *Nanotechnology* 2010;21:375301.
- [15] Spinney P, Howitt D, Collins S, Smith R. Electron beam stimulated oxidation of carbon. *Nanotechnology* 2009;20:465301.
- [16] Yuzvinsky T, Fennimore A, Mickelson W, Esquivias C, Zettl A. Precision cutting of nanotubes with a low-energy electron beam. *Appl Phys Lett* 2005;86:053109.
- [17] Liu P, Arai F, Fukuda T. Cutting of carbon nanotubes assisted with oxygen gas inside a scanning electron microscope. *Appl Phys Lett* 2006;89:113104.
- [18] Thiele C, Engel M, Hennrich F, Kappes MM, Johnsen KP, Frase CG, et al. Controlled fabrication of single-walled carbon nanotube electrodes by electron-beam-induced oxidation. *Appl Phys Lett* 2011;99:173105.
- [19] Fox D, O'Neill A, Zhou D, Boese M, Coleman JN, Zhang HZ. Nitrogen assisted etching of graphene layers in a scanning electron microscope. *Appl Phys Lett* 2011;98:243117.
- [20] Novoselov KS, Jiang D, Schedin F, Booth TJ, Khotkevich VV, Morozov SV, et al. Two-dimensional atomic crystals. *PNAS* 2005;102:10451–3.
- [21] Casiraghi C, Hartschuh A, Lidorikis E, Qian H, Harutyunyan H, Gokus T, et al. Rayleigh imaging of graphene and graphene layers. *Nano Lett* 2007;7:2711–7.
- [22] Ferrari AC, Meyer JC, Scardaci V, Casiraghi C, Lazzeri M, Mauri F, et al. Raman spectrum of graphene and graphene layers. *Phys Rev Lett* 2006;97:187401.
- [23] Das A, Pisana S, Chakraborty B, Piscanec S, Saha SK, Waghmare UV, et al. Monitoring dopants by Raman scattering in an electrochemically top-gated graphene transistor. *Nat Nanotechnol* 2008;3:210–5.
- [24] Vijayaraghavan A, Blatt S, Marquardt C, Dehm S, Wahi R, Hennrich F, et al. Imaging electronic structure of carbon nanotubes by voltage-contrast scanning electron microscopy. *Nano Res* 2008;1:321–32.
- [25] Touzin M, Goeuriot D, Guerret-Piécourt C, Juvé D, Tréheux D, Fitting HJ. Electron beam charging of insulators: a self-consistent flight-drift model. *J Appl Phys* 2006;99:114110.
- [26] Gokus T, Nair RR, Bonetti A, Böhmeler M, Lombardo A, Novoselov KS, et al. Making graphene luminescent by oxygen plasma treatment. *ACS Nano* 2009;3:3963–8.
- [27] Yang X, Tang S, Ding G, Xie X, Jiang M, Huang F. Layer-by-layer thinning of graphene by plasma irradiation and post-annealing. *Nanotechnology* 2012;23:025704.
- [28] Felten A, Flavel BS, Britnell L, Eckmann A, Louette P, Pireaux JJ, et al. Single- and double-sided chemical functionalization of bilayer graphene. *Small* 2013;9:631–9.
- [29] Schram B, Heer FD, van der Wiel M, Kistemaker J. Ionization cross sections for electrons (0.6–20 keV) in noble and diatomic gases. *Physica* 1965;31:94–112.
- [30] Rapp D, Englander-Golden P. Total cross sections for ionization and attachment in gases by electron impact. I. Positive ionization. *J Chem Phys* 1965;43:1464–79.
- [31] Itikawa Y. Cross sections for electron collisions with oxygen molecules. *J Phys Chem Ref Data* 2009;38:1–20.
- [32] Schreiber E, Fitting HJ. Monte Carlo simulation of secondary electron emission from the insulator SiO₂. *J Electron Spectrosc Relat Phenom* 2002;124:25–37.
- [33] Silvis-Cividjian N, Hagen CW, Kruit P. Spatial resolution limits in electron-beam-induced deposition. *J Appl Phys* 2005;98:1–11.
- [34] Jiang D, Sumpter BG, Dai S. Unique chemical reactivity of a graphene nanoribbon's zigzag edge. *J Chem Phys* 2007;126:134701.
- [35] Sharma R, Baik JH, Perera CJ, Strano MS. Anomalously large reactivity of single graphene layers and edges toward electron transfer chemistries. *Nano Lett* 2010;10:398–405.
- [36] Nemes-Incze P, Magda G, Kamaras K, Biro LP. Crystallographically selective nanopatterning of graphene on SiO₂. *Nano Res* 2010;3:110–6.
- [37] Reimer L. Image formation in low-voltage scanning electron microscopy; tutorial texts in optical engineering. Bellingham: SPIE Optical Engineering Press; 1993.
- [38] Postek MT. An approach to the reduction of hydrocarbon contamination in the scanning electron microscope. *Scanning* 1996;18:269–74.
- [39] Novoselov KS, Geim AK, Morozov SV, Jiang D, Zhang Y, Dubonos SV, et al. Electric field effect in atomically thin carbon films. *Science* 2004;22:666–9.
- [40] Kalceff MAS, Phillips MR, Moon AR. Electron irradiation-induced changes in the surface topography of silicon dioxide. *J Appl Phys* 1996;80:4308–14.